

Capturing Stable HDR Videos Using a Dual-Camera System

Qianyu Zhang, Bolun Zheng*, *Member, IEEE*, Lingyu Zhu, Hangjia Pan, Zunjie Zhu,
Zongpeng Li, *Senior Member, IEEE*, Shiqi Wang, *Senior Member, IEEE*

Abstract—High Dynamic Range (HDR) video acquisition using the alternating exposure (AE) paradigm has garnered significant attention due to its cost-effectiveness with a single consumer camera. However, despite progress driven by deep neural networks, these methods remain prone to temporal flicker in real-world applications due to inter-frame exposure inconsistencies. To address this challenge while maintaining the cost-effectiveness of the AE paradigm, we propose a novel learning-based HDR video generation solution. Specifically, we propose a dual-stream HDR video generation paradigm that decouples temporal luminance anchoring from exposure-variant detail reconstruction, overcoming the inherent limitations of the AE paradigm. To support this, we design an asynchronous dual-camera system (DCS), which enables independent exposure control across two cameras, eliminating the need for synchronization typically required in traditional multi-camera setups. Furthermore, an exposure-adaptive fusion network (EAFNet) is formulated for the DCS system. EAFNet integrates a pre-alignment subnetwork that aligns features across varying exposures, ensuring robust feature extraction for subsequent fusion, an asymmetric cross-feature fusion subnetwork that emphasizes reference-based attention to effectively merge these features across exposures, and a reconstruction subnetwork to mitigate ghosting artifacts and preserve fine details. Extensive experimental evaluations demonstrate that the proposed method achieves state-of-the-art performance across various datasets, showing the remarkable potential of our solution in HDR video reconstruction. The codes and data captured by DCS will be available at <https://zqqyqy.github.io/DCS-HDR/>.

Index Terms—HDR video, multi-exposure image fusion, luminance alignment

I. INTRODUCTION

Capturing the full range of illumination in high dynamic range (HDR) scenarios is a challenging task for standard digital cameras [10, 18, 29]. Thanks to the multi-exposure fusion (MEF) technology [1, 45], we can successfully capture HDR images in static scenarios by fusing multiple images of different exposure times. However, capturing HDR videos with a standard digital camera in dynamic scenes has not yet been effectively resolved [50, 51]. Early studies concentrated on designing hardware systems for directly capturing HDR video, including internal/external beam splitters [28, 39, 47], specialized sensors [7, 15, 20, 38], modular cameras [61] and neuromorphic cameras [14], *etc.* Although these solutions show good potential for capturing high-quality HDR videos,

their high cost and bulky design severely limit their widespread adoption.

The alternating exposure (AE) paradigm, first introduced by Kang *et al.* [25], enables low-cost HDR video acquisition using a single camera with rapidly switching exposures, but it also introduces challenges in maintaining temporal consistency and suppressing ghosting artifacts. Traditional AE-based methods adopt strategies such as motion-compensated fusion [13, 24] and optical flow-based reconstruction [35] to align and merge complementary exposures for HDR reconstruction, but they remain highly sensitive to motion misalignment, struggle with occlusions and non-rigid deformations, and often rely on hand-crafted heuristics that lack generalization. Recent deep learning approaches [9, 21, 54] have advanced this direction by employing deep neural architectures with stronger feature representations and learning-based alignment mechanisms. These methods have achieved promising results by training on synthetic datasets with well-structured exposure patterns and often produce temporally consistent outputs under controlled settings. However, in real-world scenarios, variations in brightness distribution caused by changes in scene content, illumination, or sensor response can disrupt the learned alignment and fusion behavior. As a result, networks that perform well in ideal conditions often suffer from temporal flickering or inconsistent reconstruction when deployed in real environments (see Fig. 1(d)).

This instability highlights a fundamental limitation of the AE paradigm itself, rather than just model design, thus leading us to explore a new solution that circumvents inter-frame exposure inconsistency. Specifically, in the AE paradigm, detail selection and global luminance determination are inherently entangled at the input level. Existing methods [9, 54] typically process both aspects within a single modeling stream, without explicit disentanglement in input design or feature representation. As a result, the network must simultaneously decide which regions to source from each exposure and how to establish the overall luminance mapping within the same representational space. As shown in Fig. 1, this tight coupling leads to feature interference and makes the learned mapping strongly dependent on the exposure patterns seen during training, thereby reducing robustness and temporal stability under distribution shifts. To address this, we propose a dual-stream generation paradigm that decouples temporal luminance anchoring from exposure-variant detail reconstruction, thereby reducing feature interference and enhancing generalization across varying exposure patterns and scene conditions. Our paradigm is meticulously designed at both the hardware system and algorithmic levels, forming a complete HDR video generation solution that supports practical deployment and robust reconstruction in real-world environments.

Qianyu Zhang, Bolun Zheng, Hangjia Pan, Zongpeng Li are with the School of Automation, Hangzhou Dianzi University, Hangzhou 310018, China (e-mail: qyzhang@hdu.edu.cn; blzheng@hdu.edu.cn; 1072272964@qq.com; zongpeng@tsinghua.edu.cn). Zunjie Zhu is with the Lishui Institute of Hangzhou Dianzi University (e-mail: zunjiezhu@hdu.edu.cn). Lingyu Zhu and Shiqi Wang are with the Department of Computer Science, City University of Hong Kong (e-mail: lingyuzhu-c@my.cityu.edu.hk; shiqiwan@cityu.edu.hk)

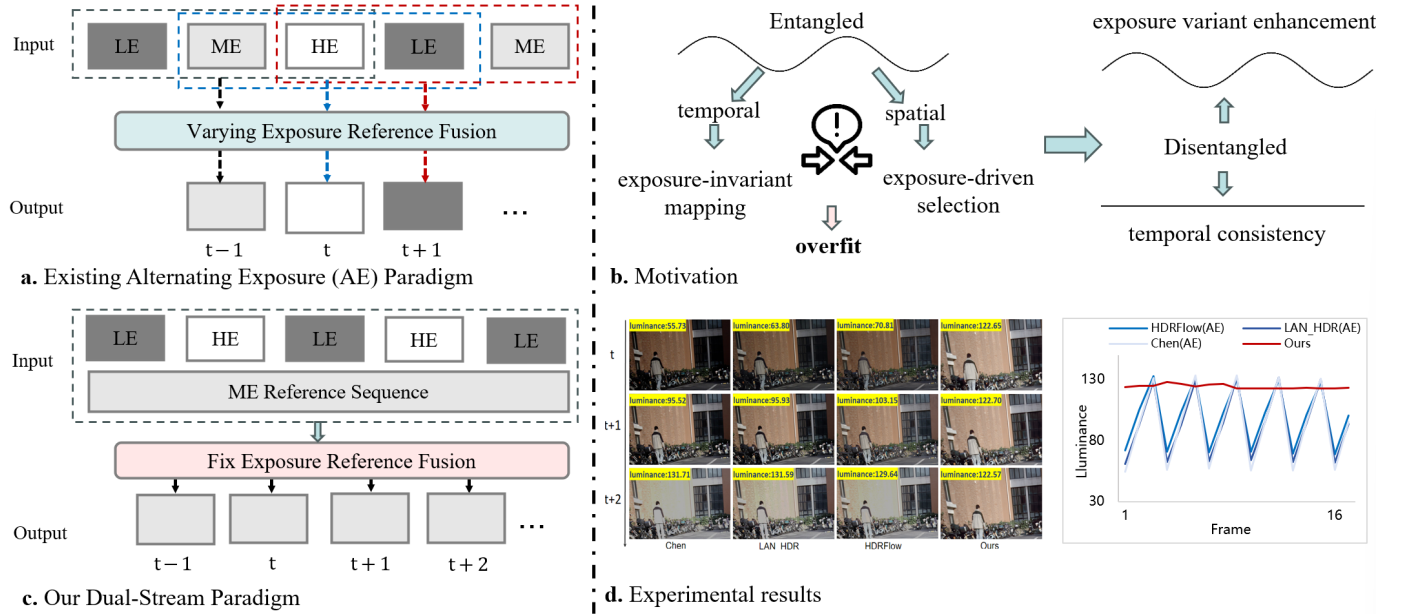


Fig. 1: Overview of challenges in the alternating exposure (AE) paradigm and our proposed dual-stream paradigm for stable HDR video generation. (a) existing AE paradigm fuses alternating exposures (LE/ME/HE) with varying reference frames, resulting in flickering artifacts (luminance fluctuations exceeding 30). (b-d) Our dual-stream paradigm employs a fixed-exposure reference sequence for stable luminance anchoring, while a separate stream handles exposure-variant enhancement, ensuring consistent illumination across reference frames, enabling temporally consistent HDR reconstruction results (luminance fluctuations limited to under 1).

Our hardware architecture is designed to implement an asynchronous dual-camera system (DCS) that capitalizes on the prevalent availability of multi-camera hardware in consumer electronic devices. Unlike prior dual-camera HDR imaging systems [11, 31] designed for static scenes under strict synchronization constraints, our DCS is tailored for dynamic video scenarios. By relaxing the synchronization requirement, it supports independent exposure control across two cameras. This design not only facilitates flexible and practical deployment without precision alignment but also avoids the frame rate bottleneck imposed by long-exposure frames in synchronized systems. As a result, our system enables high-quality HDR video capture at high frame rates. Specifically, the designed DCS system utilizes a fixed-exposure reference sequence as the temporal baseline, while simultaneously leveraging a varying-exposure stream to enrich the dynamic range. This system-level approach addresses key limitations of existing video methods. The reference stream mitigates the temporal inconsistencies and flickering commonly observed in AE-based single-camera systems, while the division of labor between the two cameras eliminates the need for precise synchronization inherent in traditional multi-camera systems, allowing for independent and flexible exposure control. Furthermore, the proposed DCS remains fully compatible with most existing image HDR deghosting algorithms, enabling temporally consistent and robust HDR video reconstruction.

Building on the proposed paradigm and DCS system, we now turn to the algorithmic level. We first revisit existing HDR deghosting approaches to extract insights and expose their limitations. Current methods can be broadly divided into

optical-flow-based [42, 44] and attention-based [34, 56] strategies. The former relies on optical flow to align inputs before fusion, which often suffers from low accuracy in estimating optical flow. On the other hand, attention-based methods, while offering greater flexibility, their attention maps are typically computed only from texture and luminance cues, without explicitly leveraging exposure information. Moreover, they generally assign equal importance to reference and non-reference frames, which allows attention to be skewed by non-reference inputs in complex scenes. In our DCS, the presence of parallax introduces additional variations between inputs, making it even more important to design attention mechanisms that emphasize reference frames. Consequently, both categories exhibit limited robustness in dynamic, exposure-varying, and parallax-affected settings, where inaccurate alignment and exposure-insensitive attention lead to ghosting and color distortion. To address this, we propose an exposure-adaptive fusion network (EAFNet) tailored for the proposed DCS system to achieve robust and generalized HDR reconstruction. Our EAFNet consists of a pre-alignment subnetwork, an asymmetric cross-feature fusion subnetwork, and a reconstruction subnetwork. The pre-alignment subnetwork consists of a global luminance alignment (GLA) and an exposure-guided feature selection module (EFSM) to leverage exposure information, enhancing meaningful details and ensuring that the most relevant features are preserved despite varying exposure levels. The asymmetric cross-feature fusion subnetwork aims to explore reference-dominated attention maps, align cross-scale features, and integrate cross-feature information to improve the fusion. Additionally, a reconstruction subnetwork is introduced to

suppress ghosting artifacts and enhance fine details.

In summary, our contributions can be summarized as follows:

- **Paradigm:** We introduce a dual-stream HDR video generation paradigm that explicitly decouples temporal luminance anchoring from exposure-variant detail reconstruction. Our approach employs a fixed-exposure stream to maintain temporal alignment across frames, while a complementary stream with varying exposures enhances the dynamic range. This design fundamentally improves temporal consistency and reconstruction stability.
- **System:** We design and implement an asynchronous dual-camera system to validate the feasibility of our proposed solution and bridge the gap between algorithmic design and practical deployment. Unlike traditional synchronized setups constrained by long-exposure frames, our system enables high-frame-rate video capture in dynamic scenes by supporting independent exposure control without requiring hardware-level synchronization. Moreover, the system seamlessly integrates with existing image deghosting methods to achieve temporally consistent video reconstruction.
- **Method:** To support our dual-camera system, we propose a novel model design, EAFNet. We leverage exposure information and explore the intrinsic properties of the images, ensuring that the most relevant features receive attention under different exposure conditions. Furthermore, we explore reference-dominated attention and effectively fuse complementary features across exposures, enabling robust representation under diverse lighting scenarios.
- **Results:** Our proposed dual-stream HDR video generation paradigm demonstrates significant advancements across multiple aspects. Through extensive qualitative and quantitative experiments, we validate the effectiveness of our contribution.

The rest of this article is organized as follows. Section II presents the related works. Section III introduces our solution for video HDR capturing and our dual-camera system. Section IV introduces the proposed EAFNet in detail. Section V presents the experimental results, and the conclusion is given in Section VI.

II. RELATED WORK

A. HDR Image Reconstruction.

1) *Traditional Methods:* Traditional multi-exposure HDR image fusion methods address the ghosting problem using two main approaches: motion-aligned-based and motion-rejection-based methods. Motion-aligned methods focus on globally aligning LDR images, followed by rejection of unaligned pixels to eliminate ghosting. Early works by Bogoni *et al.* [1] used optical flow for motion estimation, while later improvements by Kang *et al.* [25] incorporated exposure time information for enhanced alignment. Further advancements include patch-based energy minimization by Sen *et al.* [45] and luminance-based optimization by Hu *et al.* [17]. Motion-rejection methods, on the other hand, identify and exclude motion regions before fusion. Grosch *et al.* [12] and Jacobs

et al. [19] detected motion using intensity differences and weighted variance, respectively, while He *et al.* [16] and Zhang *et al.* [59] refined motion detection with graph-cut and image gradient techniques.

2) *Deep Learning Approaches:* With the rapid advancement of deep learning, neural network-based methods for HDR image reconstruction have gained significant attention and have emerged as the prevailing approach in the field. These can be categorized primarily into the following types:

Flow-based Alignment. Kalantari *et al.* [22] first applied CNNs to multi-exposure HDR imaging, using optical flow to register non-reference LDR images to a reference image. Since LDR images contain not only motion regions but also saturated regions, which do not satisfy the assumption of luminance consistency of the optical flow method, Peng *et al.* [42] and Prabhakar *et al.* [44] suggested that the typical optical flow algorithm may lead to large misalignment errors. Therefore, they used optical flow networks (e.g., FlowNet) to achieve alignment. SAFNet [27] refined valuable regions and estimated motion to produce high-quality HDR images. However, when long-distance motions occur in the LDR images, these methods still struggle to estimate the accurate flow for alignment.

Direct Feature Concatenation. Wu *et al.* [53] introduced a flow-free approach, treating HDR imaging as an image transformation problem. A similar approach was also employed in [57]. Niu *et al.* [41] and Li *et al.* [30] used Generative Adversarial Networks (GANs) for HDR reconstruction from multi-exposure LDR images with significant motion. However, they still face challenges in handling extreme motion and dynamic scenes.

Attention-based Alignment. AHDRNet [56] first introduced the attention mechanism into multi-exposure HDR reconstruction for dynamic scenes, coupling it with a densely connected dilated residual module to achieve alignment and fusion. Subsequent works focused on refining alignment strategies. Liu *et al.* [33] introduced a Pyramid Cascading Deformable (PCD) module, using multi-scale deformable convolutions for feature alignment in LDR images. Chen *et al.* [3] and DomainPlus [62] further improved fusion through progressive attention and coarse-to-fine multi-scale designs. Transformer-based methods such as HDR-Trans [34], Chen *et al.* [4], and HyHDRNet [55] integrated global context modeling into HDR pipelines, enhancing feature representation. SCTNet [46] combined spatial and channel attention to improve semantic consistency. Despite advances in these approaches, most existing methods lack explicit modeling of exposure variations, resulting in sensitivity to brightness variations. Moreover, treating reference and non-reference frames equally during fusion often leads to ghosting artifacts, particularly in high-contrast regions dominated by non-reference content.

Dual-lens-based system. Dual-lens HDR imaging leverages paired images with different exposures to synthesize high-quality HDR content. Dong *et al.* [11] and Li *et al.* [31] align features under the assumption of simple 1D parallax between rectified stereo pairs. While effective under controlled conditions, both frameworks assume the only misalignment present is 1D parallax between image pairs. This assumption is embedded in their data collection and rectification procedures,

simplifying alignment to left–right disparities but limiting their ability to model more complex distortions. In dynamic scenes, mismatched exposure times introduce complex misalignments, including motion blur in long-exposure frames that cannot be captured by disparity-based alignment alone.

B. HDR Video Reconstruction

Dedicated Hardware Solutions. Dedicated hardware solutions, such as single-pixel imaging [40], scanline exposure/ISO [7], internal [47] or external beam splitters [39], as well as residue cameras [61] and neuromorphic vision cameras [14], are capable of rapidly and efficiently generating detailed HDR images or videos on specialized devices. However, the complexity and high cost of these hardware solutions limit their widespread adoption.

Traditional Methods. Most HDR video reconstruction methods utilize alternating exposure sequences to align multiple frames for HDR video reconstruction. Kang *et al.* [25] introduced the first algorithm in this category, employing global and local registration to align multi-exposure images at each time step and merge them into a single HDR frame. Mangiat *et al.* [35] applied block-based motion estimation with refined motion vectors and later improved this method with HDR filtering to eliminate block artifacts [36]. Additionally, Gryaditskaya *et al.* [13] proposed an adaptive weighting algorithm to minimize motion artifacts. Li *et al.* [32] proposed a statistical method to avoid exact alignment estimation. However, these methods are typically time-consuming and often introduce visible artifacts.

Deep Learning Methods. Kalantari *et al.* [21] proposed the first deep learning-based method for generating HDR video from alternating exposure sequences. Chen *et al.* [2] developed a two-stage coarse-to-fine framework that integrated deformable convolutions with HDR video reconstruction. LAN-HDR [8] aligned adjacent frames with the reference frame using luminance-based attention scores. HDRFlow [54] designed an efficient flow network with multi-scale large kernels to handle large motions. Cui *et al.* [9] introduced exposure completion for neural HDR rendering, using feature interpolation and a novel decoding architecture to improve HDR video reconstruction. Nonetheless, alternating exposure setups inherently introduce brightness inconsistencies across reference frames, leading to temporal instability in the reconstructed video. In contrast, our design adopts a fixed-exposure reference strategy, which naturally preserves brightness consistency and mitigates flickering artifacts.

III. DUAL-CAMERA SYSTEM FOR CAPTURING HDR VIDEO

Overview. An inexpensive mainstream solution for HDR video reconstruction is generating video from image sequences captured at alternating exposure levels [9, 21, 54]. However, this approach inherits the exposure limitations of the reference frame, often resulting in visible artifacts and temporal flickering in the generated video, significantly constraining its practical application. To address this, we propose a dual-stream paradigm supported by a dual-camera system (as

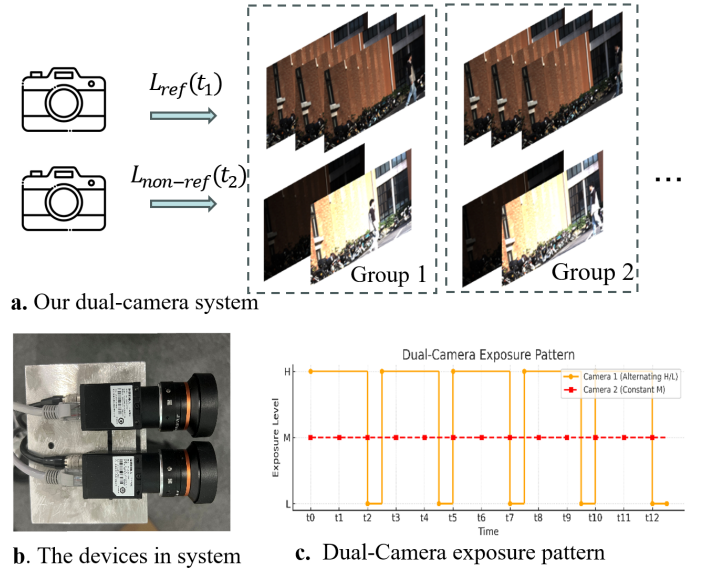


Fig. 2: Visualization of our dual-camera system. The primary camera captures continuous medium-exposure sequences as reference for temporal consistency, while the secondary camera alternates between low- and high-exposure to provide complementary information for reconstruction.

shown in Fig. 2), where the primary camera continuously captures medium-exposure frames to ensure temporal consistency, while the secondary camera captures low-exposure and high-exposure frames to provide complementary information.

A. Dual-Camera System

System Configuration. Our system employs two MV-CS032-10GC industrial cameras, which provide low-level access to operational controls for precise adjustment of exposure time and shooting strategies. Both cameras are equipped with identical lenses and are mounted side by side, secured by a mechanical support structure to ensure their relative positions remain stable throughout the imaging process.

Dual-Camera Calibration. To eliminate distortion and ensure alignment, we perform camera calibration using a checkerboard pattern. Intrinsic and extrinsic parameters are computed from images captured by the dual cameras using the camera calibration toolbox [60]. The calibration parameters are then applied to register the images, resulting in the final aligned images. This reduces potential errors and improves the subsequent processing steps.

Video Capture and System Design. Our dual-camera system employs two identical cameras with resolution $w \times h$. In practical operation, the cameras are run asynchronously: one continuously records a medium-exposure reference sequence $L_{ref}(t_1)$ to provide temporally consistent baseline frames, while the other alternates between low and high exposures $L_{non-ref}(t_2)$ to supply the luminance diversity required for dynamic range expansion. To leverage the information from two sequences, we construct approximate pairings using timestamp metadata: as shown in Fig. 2(a), for each low/high exposure pair in the alternating stream, we gather reference

frames falling within its defined temporal neighborhood and combine each of them with the same low/high pair to form input groups, enabling the reuse of one low/high pair across multiple reference frames. This pairing does not require frame-level precision, as the scenes are inherently dynamic and minor temporal offsets have a negligible impact on multi-exposure fusion. Each input group is then fed into the network to reconstruct HDR video at the same frame rate as $L_{ref}(t_1)$.

Overall, the design formulates the task as multi-exposure HDR fusion for dynamic scenes, leveraging the consistent exposure of the reference sequence to eliminate the need for luminance alignment between neighboring frames. Existing HDR image deghosting methods can be seamlessly extended to achieve consistent luminance results. To address challenges from video data and the variability of real-world scenes, we propose EAFNet, a more robust network, detailed in Section IV.

B. Further Discussion

To further clarify our contributions, we discuss the proposed paradigm from three perspectives:

1) *Relationship with Previous HDR video pipelines:* Traditional HDR video generation methods often rely on specialized sensors or expensive camera setups, such as Quad-Bayer sensors [20], Beam Splitter systems [28], etc. These methods produce high-quality HDR output through specialized hardware designs for capturing frames with different exposures, but come with significant hardware costs and are typically limited to high-end applications. In contrast, our dual-stream paradigm not only lowers hardware costs but also enhances flexibility, making it feasible for HDR video generation on consumer-grade devices.

Additionally, many existing methods address hardware limitations by employing alternating exposure techniques [2, 8, 54], where a single consumer-grade camera alternates between different exposure levels to capture HDR video. Our paradigm retains the cost-effectiveness of traditional AE methods while also addressing key challenges such as temporal consistency and robustness in real-world dynamic imaging scenarios.

2) *Relationship with Previous dual-camera systems:* Dual-camera systems have been used in HDR imaging [11, 31], but they typically require strict synchronization, which is challenging in dynamic video scenes due to exposure differences between cameras, leading to ghosting artifacts. In contrast, our system performs exposure fusion without synchronization, enabling better adaptability to dynamic environments. Additionally, while synchronized systems are constrained by long exposure times that lower frame rates, our system decouples temporal stability from exposure variation, allowing flexible exposure settings and maintaining high frame rates. The reference stream controls the frame rate, making our system particularly suited for high-frame-rate HDR video capture, especially in low-light conditions.

Beyond HDR imaging, dual-camera frameworks have also been explored in related video enhancement tasks. For instance, Cheng *et al.* [5] and H2-Stereo [6] proposed dual-camera super-resolution systems that pair a high-resolution

low-frame-rate stream with a low-resolution high-frame-rate stream to reconstruct videos with high spatiotemporal resolution. Similarly, dual-camera designs have been applied in video de-moiré [49]. While these methods also exploit asymmetric information across cameras, their optimization targets are fundamentally different from ours: they generally assume consistent exposure between cameras and focus on improving spatial or temporal fidelity, rather than expanding dynamic range. In contrast, our framework introduces an exposure-asymmetric dual-camera configuration: a reference camera maintains a stable mid-level exposure to anchor temporal consistency, while an auxiliary camera alternates between low and high exposures to provide extreme luminance details. This design effectively decouples temporal stability from exposure diversity, a direction not explored in prior work. Furthermore, we relax the requirement for frame-level synchronization by adopting group-wise asynchronous fusion, where multiple reference frames are paired with an alternating-exposure pair from the auxiliary camera and jointly processed by a dedicated deghosting network. This pipeline enables high-frame-rate HDR video capture with minimal flicker, a capability not achievable with single-camera alternating exposure or conventional dual-camera systems designed for other tasks.

In addition, our system exhibits high scalability and strong generalization capability. It does not rely on device-specific calibration or training data. Instead, multi-exposure fusion models trained on publicly available datasets can be seamlessly integrated into our framework without any retraining or fine-tuning. Leveraging this flexibility, our system can directly produce flicker-free HDR videos from real-world captures. In contrast, existing dual-camera HDR solutions typically require carefully calibrated camera pairs and task-specific training, which significantly restricts their deployment in practical scenarios. To the best of our knowledge, none of the prior methods provide such plug-and-play adaptability while maintaining high temporal stability.

3) *The advantages of the proposed video generation paradigm:* The proposed video generation paradigm offers several distinct advantages. First, the dual-stream design introduces an exposure-asymmetric configuration that explicitly decouples temporal stability from exposure diversity. This principle alleviates the feature interference inherent in AE-based HDR systems and improves robustness in dynamic real-world environments.

Second, the paradigm offers flexibility in exposure scheduling and frame rate control. By anchoring the output frame rate to the reference stream, the system can deliver high-frame-rate HDR video while simultaneously leveraging the auxiliary stream for extended dynamic range, which is particularly beneficial in low-light or high-motion conditions. In this asynchronous dual-stream capture scheme, the reference stream follows standard auto-exposure to provide a stable baseline, while the auxiliary stream operates at a lower frame rate with fixed or preset exposures. Such a design improves energy efficiency and reduces bandwidth and storage overhead, enabling seamless integration with standard video encoding and transmission protocols.

Third, the paradigm achieves strong scalability and gener-

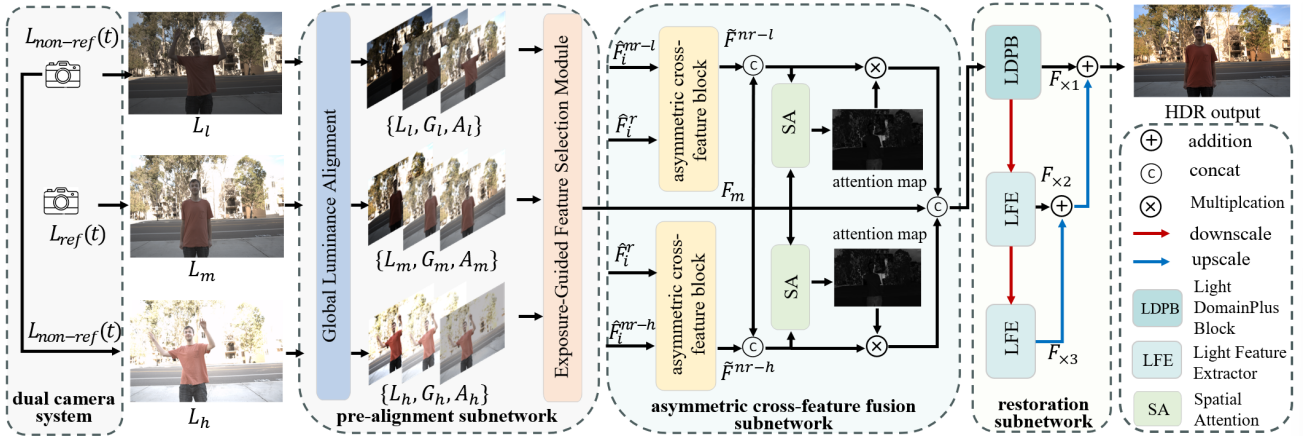


Fig. 3: The architecture of EAFNet consists of a pre-alignment subnetwork, an asymmetric cross-feature fusion subnetwork, and a restoration subnetwork. We introduce GLA and EFSM to leverage exposure information, explore the intrinsic properties of the images, and help preserve finer details across varying exposures. The asymmetric cross-feature fusion subnetwork improves image fusion by aligning cross-scale features and performing cross-feature fusion. The reconstruction subnetwork adopts a multi-scale architecture to reduce ghosting and refine features at different resolutions.

alization. Multi-exposure fusion models trained on publicly available datasets can be directly applied without device-specific calibration or retraining, enabling plug-and-play deployment.

Finally, the design is highly practical for integration into consumer-grade devices. Existing multi-camera systems can readily adopt the dual-stream setup without the need for specialized sensors or costly calibration procedures, broadening the accessibility of HDR video capture.

IV. METHOD

A. Overview

In this section, we introduce the overall framework of the proposed EAFNet, built upon a pre-alignment subnetwork (in Sec. IV-B), an asymmetric cross-feature fusion subnetwork (in Sec. IV-C) and a restoration subnetwork (in Sec. IV-D).

As shown in Fig. 3, the pre-alignment subnetwork aims to improve detail preservation and color accuracy by exploring exposure information and extracting meaningful features from the non-reference image. It incorporates Global Luminance Alignment (GLA) to ensure consistent brightness across varying exposures, and an Exposure-guide Feature Selection Module (EFSM) to identify and focus on the most relevant regions based on the exposure information. These mechanisms work together to enhance the input features before fusion. Next, the asymmetric cross-feature fusion subnetwork plays a critical role in blending features from different exposures while emphasizing the most important details. It processes the low- and high-exposure inputs through separate asymmetric cross-feature fusion blocks, each built with a multi-scale design. The fusion is driven by an Asymmetric Cross-Attention (ACA), which leverages reference-dominated attention maps to improve the alignment of query and key features, facilitating more effective feature propagation across multiple scales. Finally, the restoration subnetwork addresses common issues such as ghosting artifacts. It is designed to suppress ghosting while preserving fine details at multiple scales.

B. pre-alignment subnetwork

The pre-alignment subnetwork aims to extract meaningful details from the non-reference image by leveraging exposure information. GLA is introduced to maintain consistent luminance across varying exposures, while the EFSM explores the correlation between inputs and exposure to focus on the most relevant regions for fusion.

Global Luminance Alignment (GLA). Following established HDR reconstruction pipelines [23, 56], we employ three LDR images $\{L_l, L_m, L_h\}$ (sorted by their exposure length) as input. These images are first mapped to the HDR domain relying on gamma correction [23] to produce a set of gamma-corrected images G_i , where $i \in \{l, m, h\}$ and $\gamma = 2.2$.

To reduce inter-exposure luminance discrepancies and improve alignment robustness, we introduce GLA in the pre-alignment stage. GLA operates in the sRGB domain and ensures consistent luminance distributions across inputs and minimizes exposure-induced mismatches during fusion. Formally, for each non-reference LDR image L_i , global alignment is performed as:

$$A_i = \text{clip}\left(L_i \times \frac{\mathbb{E}(L_m)}{\mathbb{E}(L_i)}, 0, 1\right), \quad i \in \{l, h\}, \quad (1)$$

where A_i denotes the luminance-aligned image, $\mathbb{E}(\cdot)$ computes the average luminance, and $\text{clip}(\cdot, 0, 1)$ restricts pixel values to the valid dynamic range. Since the mid-exposure image L_m serves as the reference, we set $A_m = L_m$.

As shown in Fig. 3, given a set of LDR images with varying exposure times, we construct the input tensor $\mathbf{L}_{\text{in}} = (\{L_l, G_l, A_l\}, \{L_m, G_m, A_m\}, \{L_h, G_h, A_h\})$, where each triplet (L_i, G_i, A_i) represents the original, gamma-corrected, and GLA-processed versions of the image under exposure setting $i \in \{l, m, h\}$. This tensor is then passed to the EFSM for feature selection and alignment refinement.

Exposure-guided Feature Selection Module (EFSM). Exposure information is crucial for distinguishing the reliability

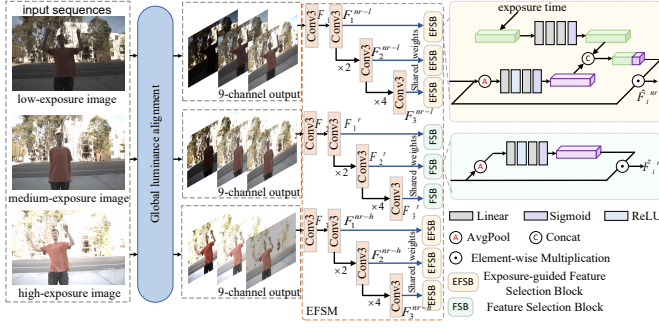


Fig. 4: The pre-alignment subnetwork is composed of two parts: global luminance alignment (GLA) and exposure-guided feature selection module (EFSM). The input is divided into multiple scales using a 3×3 convolution, with a shared-weight feature selection block applied at each scale.

and detail across different exposures. For the obtained multi-channel features, we propose the EFSM, which consists of the Exposure-guided Feature Selection Block (EFSB) and the Feature Selection Block (FSB). EFSM introduces exposure-aware modulation based on relative exposure priors, selectively emphasizing well-exposed regions and suppressing unreliable features, thereby ensuring more reliable feature representation for fusion.

Specifically, EFSM operates in a multi-scale feature refinement architecture, as depicted in Fig. 4. Given a 9-channel composite input tensor \mathbf{L}_{in} , we first extract three initial feature maps $\{\mathbf{F}_l, \mathbf{F}_m, \mathbf{F}_h\}$ via parallel 3×3 convolutional layers. For subsequent processing clarity, we formally define $\mathbf{F}^{nr} \triangleq \{\mathbf{F}_l, \mathbf{F}_h\}$ as non-reference features and $\mathbf{F}^r \triangleq \mathbf{F}_m$ as reference features. These are fed into two distinct but weight-shared selection blocks: EFSB for non-reference features and FSB for reference features.

To encode exposure priors, we normalize the exposure times $\{t_l, t_m, t_h\}$ relative to the middle exposure as:

$$e_l = \log_2\left(\frac{t_l}{t_m}\right) \cdot c, \quad e_h = \log_2\left(\frac{t_h}{t_m}\right) \cdot c, \quad (2)$$

where e_l and e_h represent the relative exposure embeddings for the low- and high-exposure branches, respectively, and c is a hyper-parameter empirically set to 0.1.

Both \mathbf{F}^r and \mathbf{F}^{nr} are processed through global average pooling followed by two fully connected layers and a sigmoid activation, producing feature-based modulation vectors: $\mathbf{v}^{nr} \in \mathbb{R}^{1 \times 1 \times 64}$ and $\mathbf{v}^r \in \mathbb{R}^{1 \times 1 \times 64}$. In parallel, the exposure inputs e_l, e_h are passed through a shared fully connected layer to obtain exposure-based modulation vectors $\mathbf{v}^t \in \mathbb{R}^{1 \times 1 \times 128}$. To combine feature reliability and exposure priors, we compute the exposure-guided modulation weights as:

$$\mathbf{u}^{nr} = \sigma(\text{FC}_3([\mathbf{v}^{nr}; \mathbf{v}^t])), \quad (3)$$

where $[\cdot; \cdot]$ denotes channel-wise concatenation, $\sigma(\cdot)$ is sigmoid activation, and $\text{FC}_3(\cdot)$ represents three fully connected layers. Finally, the refined features are obtained by reweighting:

$$\hat{\mathbf{F}}_i^r = \mathbf{F}_i^r \odot \mathbf{v}^r, \quad \hat{\mathbf{F}}_i^{nr} = \mathbf{F}_i^{nr} \odot \mathbf{u}^{nr}, \quad (4)$$

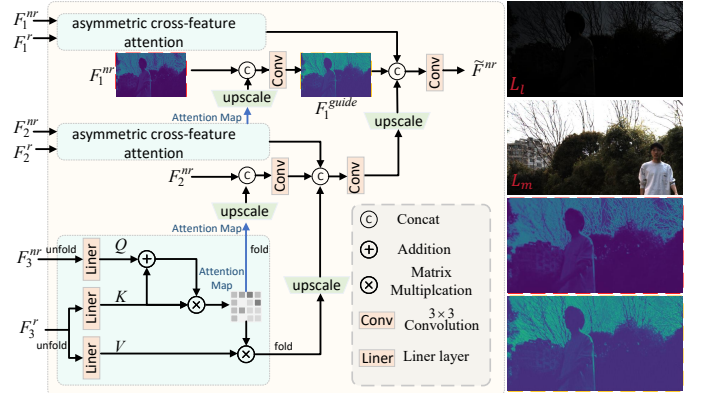


Fig. 5: The structure of the asymmetric cross-feature fusion block. It employs asymmetric cross-feature attention to align reference and non-reference features, integrating coarse-to-fine guidance for enhanced reference-dominated feature fusion and improved HDR reconstruction.

where \odot denotes element-wise multiplication.

C. asymmetric cross-feature fusion subnetwork

One of the central challenges in multi-exposure fusion lies in leveraging the complementary details from non-reference images without introducing ghosting artifacts, particularly in the presence of large motion or occlusions [34, 58]. While non-reference inputs offer richer information in under-/over-exposed regions, they also carry a higher risk of misalignment. To address this, we propose an asymmetric cross-feature fusion subnetwork, which employs asymmetric cross-feature fusion blocks to selectively align and fuse cross-exposure features in a coarse-to-fine manner. Each fusion block is centered around the Asymmetric Cross-Attention (ACA) module, which leverages reference-dominant attention to fuse features.

As illustrated in Fig. 5, the proposed module adopts a multi-scale architecture, where local attention at each level is computed via an ACA mechanism. At each scale $i \in \{1, 2, 3\}$, we first unfold the refined reference features $\hat{\mathbf{F}}_i^r$ and non-reference features $\hat{\mathbf{F}}_i^{nr}$ into patch tokens using a window-based unfolding operator $\phi(\cdot)$. The attention is formulated in an asymmetric manner, where queries are derived from the reference stream, while keys and values are obtained from the non-reference stream to facilitate reference-guided feature aggregation. To further emphasize reference dominance, we incorporate query features into the key projection via additive modulation:

$$\mathbf{M}_i = \text{softmax}\left(\left(\mathbf{Q}_i + \mathbf{K}_i\right)\mathbf{K}_i^\top / \sqrt{C}\right), \quad (5)$$

where $\mathbf{Q}_i = \phi(\hat{\mathbf{F}}_i^r) \mathbf{W}_i^q$ and $\mathbf{K}_i, \mathbf{V}_i = \phi(\hat{\mathbf{F}}_i^{nr}) \mathbf{W}_i^{k,v}$, with $\mathbf{W}_i^{q,k,v}$ being learnable matrices. This asymmetric formulation encourages stronger alignment toward the reference features and reduces the impact of unreliable non-reference content. Then, the aligned non-reference features \mathbf{F}_i^{anr} are obtained by applying a folding operation to the result of the multiplication of \mathbf{M}_i and \mathbf{V}_i .

To enhance fine-scale alignment with global context, we incorporate a cross-scale guidance mechanism. Specifically,

attention information from the coarser scale $i + 1$ is projected and injected into the finer scale i as:

$$\mathbf{F}_i^{\text{guid}} = \text{Conv}_{3 \times 3}([\mathbf{F}_i^{\text{nr}}; U(\psi(\mathbf{M}_{i+1}))]), \quad 1 \leq i < N, \quad (6)$$

where $\text{Conv}_{3 \times 3}(\cdot)$ denotes a 3×3 convolution, N denotes the number of refinement scales, $U(\cdot)$ is pixel shuffle upsampling, and $\psi(\cdot)$ represents the projection of attention from the coarser scale. Then, $\mathbf{F}_i^{\text{guid}}$ injects reference-dominated attention to facilitate multi-scale alignment. The output of the ACA \mathbf{F}^{nr} is computed by merging the aligned features from multiple scales, combining the finer-scale features with guidance from the coarser scales to produce a refined feature representation.

Finally, we generate a spatial attention map using $\tilde{\mathbf{F}}^{\text{nr}}$ and \mathbf{F}^{ref} and get the fusion output.

D. restoration subnetwork

As shown in Fig. 3, the restoration subnetwork is designed to suppress ghosting artifacts while preserving fine details across multiple scales.

Each scale begins with a Discrete Wavelet Transform (DWT) to decompose features into frequency subbands. At the lowest scale, where high-frequency details such as textures and residual motion artifacts are most prominent, we apply a Lightweight DomainPlus Block (LDPB) to perform frequency-specific corrections. The LDPB is adapted from [62] by removing dense connections to reduce complexity while retaining frequency modeling capacity.

In contrast, higher scales capture more global and low-frequency content. These layers are processed using a simple 1×1 convolution after DWT, which is sufficient for coarse structure refinement without the need for full spectral filtering. All features are subsequently reconstructed using the Inverse Wavelet Transform (IWT).

The refined features from each scale are fused in a top-down manner using upsampling and residual connection to produce the final HDR output.

E. Loss Function

HDR images are typically displayed after tone mapping. To enhance training performance, we apply the μ -law transformation, as proposed in [22], to map the HDR image from the linear domain to the tone-mapped domain, thereby improving model performance during training, the μ -law transformation can be expressed as:

$$\tau(\mathcal{H}) = \frac{\ln(1 + \mu\mathcal{H})}{\ln(1 + \mu)} \quad (7)$$

where μ is a hyperparameter set to 5000.

We adopt the L1 loss as the basic loss function for pixel-wise supervision. To correct each frequency component and enhance the training of the restoration subnetwork, we adopt the dilated advanced Sobel loss (D-ASL) loss function [63] as an additional function, which is defined as:

$$\mathcal{ASL}(\hat{Z}, Z) = \frac{1}{N} \sum | \text{Sobel}^*(\hat{Z}) - \text{Sobel}^*(Z) | \quad (8)$$

$$\mathcal{D} - \mathcal{ASL}^{\{d_1, d_2, \dots, d_n\}} = \sum_{i=1}^n \mathcal{ASL}|_{\text{dilation_rate}=d_i} \quad (9)$$

where the N is the batchsize of training, Z and \hat{Z} represent the groundtruth and the output image predicted by network after the μ -law function, Sobel^* denotes the advanced sobel filtering, and $\mathcal{ASL}|_{\text{dilation_rate}=d_i}$ denotes the ASL with a dilation rate of d_i . Following [63], we apply the reference settings that $D = \{1, 2, 3\}$ to formulate the D-ASL. Then the final loss function can be expressed as:

$$\mathcal{L}_{\text{total}} = \mathcal{L}_1(\hat{Z}, Z) + \lambda \cdot \mathcal{D} - \mathcal{ASL}^D(\hat{Z}, Z) \quad (10)$$

where $\lambda = 0.25$ is a hyper-parameter to balance the L1 loss and D-ASL.

V. EXPERIMENTS

In this section, we conduct extensive experiments to evaluate the performance of our proposed dual-stream paradigm in HDR video generation. Our dual-stream paradigm, supported by a dual-camera system and the EAFNet model, aims to address key challenges in HDR video reconstruction, such as temporal luminance consistency and spatial deghosting.

First, in Section V-A, we outline the experimental setup, including details on the training process, datasets, baseline methods, and evaluation metrics. In Section V-B, we focus on dynamic HDR image fusion, presenting both quantitative and qualitative comparisons with state-of-the-art HDR image deghosting methods to validate the effectiveness of our method in single-frame spatial fusion and deghosting. Section V-C shifts to HDR video reconstruction, where we assess the advantages of our paradigm in temporal consistency and flicker suppression, comparing it with existing AE paradigms and further validating the benefits of the EAFNet model within our proposed paradigm. Section V-D presents an ablation study, analyzing the impact of the dual-camera system configuration and the contributions of each EAFNet component. Finally, Section V-E discusses the limitations of the proposed paradigm, including the effects of camera parallax and system efficiency, and highlights potential directions for future improvements.

A. Experiment Settings

Training Details. The proposed method is implemented in PyTorch on an NVIDIA RTX4090 GPU. For the convolutional layers, we employ 64 kernels of size 3×3 with a stride of one, applying zero padding to preserve the dimensions of the resulting feature maps. The optimization is performed using the Adam optimizer [26] with an initial learning rate of 10^{-4} , and the training concludes when the learning rate reaches 10^{-6} . To train the model, both the LDR and corresponding images are cropped into 256×256 patches. A batch size of 16 is utilized during training. Patches are randomly rotated for data augmentation to avoid overfitting during the training stage.

Datasets. High-quality HDR video datasets suitable for supervised training or frame-wise quantitative evaluation are scarce, as most lack per-frame HDR ground truth and sufficient exposure diversity. To fairly and comprehensively evaluate our method, we separate the evaluation into two complementary parts: (1) **Spatial evaluation** focuses on single-frame fusion

TABLE I: Comparison results on Kalantari’s dataset and Prabhakar’s dataset. Throughout this paper, the best and second-best results of each case are highlighted in **bold red** and underlined blue, respectively.

Method	dataset setting	train and test on Kalantari’s dataset					train and test on Prabhakar’s dataset				
	metrics	PSNR- μ (\uparrow)	PSNR-L (\uparrow)	SSIM- μ (\uparrow)	SSIM-L (\uparrow)	HDR-VDP-2 (\uparrow)	PSNR- μ (\uparrow)	PSNR-L (\uparrow)	SSIM- μ (\uparrow)	SSIM-L (\uparrow)	HDR-VDP-2 (\uparrow)
Kalantari(CGF 2017) [23]		42.74	41.22	0.9877	0.9848	60.51	35.63	32.50	0.09613	0.9692	59.42
AHDRNet(CVPR 2019) [56]		43.77	41.35	0.9907	0.9859	62.30	38.61	35.26	0.9663	0.9794	61.14
Prabhakar(ECCV 2020) [43]		43.08	41.68	-	-	62.21	38.30	34.98	0.9702	0.9781	-
HDR-Trans(ECCV 2022) [34]		44.28	<u>42.88</u>	0.9916	0.9884	66.03	<u>41.31</u>	<u>39.44</u>	<u>0.9726</u>	<u>0.9885</u>	<u>63.01</u>
DomainPlus(MM 2022) [62]		44.02	41.28	0.9910	0.9864	62.91	40.38	38.08	0.9698	0.9872	62.12
SCTNet(ICCV 2023) [46]		44.13	42.12	0.9916	0.9890	66.65	41.23	38.75	0.9724	0.9881	62.29
SAFNet(ECCV 2024) [27]		<u>44.61</u>	43.09	<u>0.9918</u>	<u>0.9892</u>	<u>66.93</u>	40.18	37.90	0.9705	0.9865	62.04
EAFNet(Ours)		44.69	42.19	0.9920	0.9895	68.35	41.80	40.13	0.9731	0.9895	63.53

TABLE II: Cross-dataset evaluation on Kalantari’s dataset and Prabhakar’s dataset.

Method	dataset setting	train on Kalantari’s dataset, test on Prabhakar’s dataset				train on Prabhakar’s dataset, test on Kalantari’s dataset			
	metrics	PSNR- μ (\uparrow)	PSNR-L (\uparrow)	SSIM- μ (\uparrow)	SSIM-L (\uparrow)	PSNR- μ (\uparrow)	PSNR-L (\uparrow)	SSIM- μ (\uparrow)	SSIM-L (\uparrow)
AHDRNet(CVPR 2019) [56]		33.96	32.46	0.9601	0.9542	40.03	36.71	0.9855	0.9758
HDR-Trans(ECCV 2022) [34]		34.07	36.62	0.9675	0.9656	<u>41.38</u>	<u>39.21</u>	0.9890	0.9873
DomainPlus(MM 2022) [62]		32.64	30.42	0.9046	0.9074	41.15	38.18	0.9873	0.9837
SCTNet(ICCV 2023) [46]		33.83	30.95	0.9584	0.9521	40.88	37.59	0.9892	0.9842
SAFNet(ECCV 2024) [27]		<u>38.00</u>	<u>34.65</u>	0.9597	<u>0.9793</u>	40.86	37.50	0.9882	0.9810
EAFNet(Ours)		39.26	35.99	0.9707	0.9848	42.02	39.38	0.9903	<u>0.9870</u>

accuracy using HDR image datasets with reliable ground truth, enabling objective comparison in reconstruction quality. We assess single-frame fusion quality using three widely used HDR image datasets: Prabhakar’s dataset [44], Kalantari’s dataset [22], and Tursun’s dataset [48],

- Prabhakar’s Dataset. Including 466 training samples and 116 testing samples, with exposure values between -3EV and +3EV.
- Kalantari’s dataset. Including 74 training samples and 15 testing samples. Each consists of three LDR images, with exposure values of $\{-2 \text{ EV}, 0 \text{ EV}, +2 \text{ EV}\}$ or $\{-3 \text{ EV}, 0 \text{ EV}, +3 \text{ EV}\}$.
- Tursun’s dataset. Lacking ground truth, is used to assess the generalization ability of the models.

(2) **Temporal evaluation** focuses on luminance consistency and flicker suppression in dynamic scenes, which cannot be assessed using static image datasets. To enable a comprehensive comparison of our dual-stream HDR video generation paradigm against the widely adopted AE paradigm, we construct dedicated datasets tailored to each paradigm under real-world scenes using our DCS. This approach is necessary because the two paradigms differ fundamentally in their acquisition strategies; a direct comparison using identical inputs would be inherently unfair.

Specifically, we capture two synchronized video streams for each scene using two identical cameras (resolution 960×540). This synchronization is applied only during data acquisition to minimize scene variations between paradigms. In practical deployment, our dual-camera system operates asynchronously without hardware-level synchronization (see Section III). The first camera follows an alternating exposure pattern, and the second camera continuously captures medium-exposure frames. Our paradigm uses the low- and high-exposure frames from the first camera together with the medium-exposure frames from the second camera to reconstruct HDR video. For the AE pipeline, only the alternating exposure sequence from the first camera is used, emulating the standard AE pipeline.

We capture 26 real-world scenes under matched conditions for both datasets, covering diverse scenarios including

indoor/outdoor environments, day/night lighting, and challenging situations such as low-light, high-contrast scenes, object motion, and occlusions. Exposure settings are fixed to $(-2, 0, +2)$ or $(-1, 0, +1)$ EV to ensure sufficient exposure diversity across varying lighting conditions. This paired capture protocol guarantees that both paradigms are evaluated on scene-matched content while preserving their respective optimal acquisition strategies. However, since the dataset is captured in real-world scenes, there are two challenges in ensuring a fair comparison. First, slight parallax exists between the two camera streams, as the cameras are not perfectly aligned. To mitigate this, we capture predominantly long-range scenes, which minimize the impact of parallax. Second, temporal asynchrony arises from the exposure duration differences inherent in the AE settings. This asynchrony is a fundamental aspect of the AE paradigm and cannot be avoided. With these considerations, our paired capture protocol ensures that both paradigms are evaluated on scene-matched content while preserving their respective optimal acquisition strategies. **Baselines.** We quantitatively and qualitatively compare our EAFNet to several state-of-the-art HDR image dehazing methods including Kalantari [23], AHDR [56], Prabhakar [43], HDR-Transformer [34], SCTNet [46], DomainPlus [62], and SAFNet [27]. For fairness, we exclude few-shot and unsupervised methods that are not designed for supervised multi-exposure HDR reconstruction.

We further compare our proposed framework with representative AE-based HDR video reconstruction methods, including HDRFlow [54], LAN-HDR [8], and DeepHDRVide [2]. Due to differences in system assumptions and training strategies, AE methods are trained on their respective public datasets following the official configurations, while our method is trained on the publicly available Prabhakar dataset. All models are evaluated on the same real-world video sequences captured using our dual-camera system.

Metrics. We quantitatively evaluate the predicted HDR images by measuring PSNR and SSIM [52] in both the linear domain (-L) and the tone-mapped domain ($-\mu$) [22]. The tone mapping operation is described in Sec. IV-E. Additionally, we

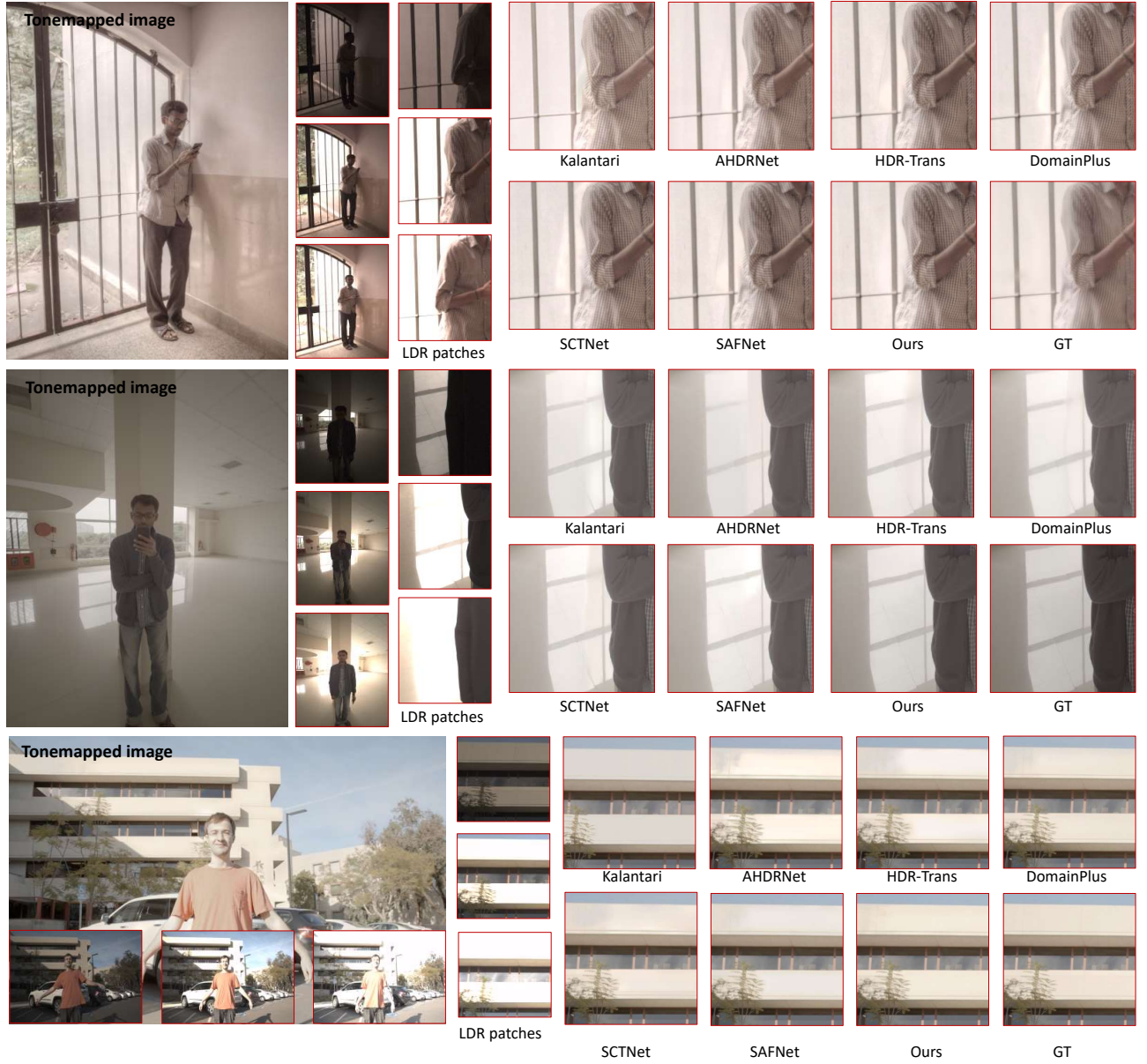


Fig. 6: Visual comparison on Kalantari's and Prabhakar's dataset. While other methods suffer from detail loss, overexposed patches, and color inconsistencies, our approach successfully reconstructs overexposed details and preserves natural, consistent color.

compare the results using HDR-VDP-2 [37] for conforming the human visual perception. We also quantitatively evaluated the luminance consistency of the video by testing the Luminance Standard Deviation (LSD), temporal SSIM (t-SSIM) and average luminance (L_{avg}):

- Average Luminance (L_{avg}):

$$L_{avg} = \frac{1}{N} \sum_{i=1}^N L_i \quad (11)$$

where N represents the number of the frame, L_i represents the mean luminance value of frame i .

- Luminance Standard Deviation (LSD):

$$LSD = \sqrt{\frac{1}{N} \sum_{i=1}^N (L_i - L_{avg})^2} \quad (12)$$

where L_i is the mean luminance of frame i .

B. HDR Image Experimental Results

Quantitative Comparisons. Table I reports the intra-dataset evaluation results on Prabhakar's and Kalantari's datasets. Our EAFNet consistently achieves the best performance across both datasets. On the Kalantari dataset, it surpasses the second-best method by 0.08 dB in PSNR- μ , while on the Prabhakar dataset, the margin increases to 0.49 dB. These gains are

TABLE III: Comparison on self-captured videos. * indicates HDR image dehghosting methods under the alternating exposure solution. The reported time refers to the inference time for a 128×128 patch on a single RTX 4090 GPU.

Method	Paradigm	LSD (\downarrow)	t-SSIM (\uparrow)	L_{avg}	Inference time (ms, \downarrow)
DeepHDRVideo(ICCV 2021) [2]	alternating-exposure paradigm	0.1031	0.5913	105.02	22.23
LAN-HDR(ICCV 2023) [8]		0.1003	0.6879	108.75	21.69
HDRFlow(CVPR 2024) [54]		0.0914	0.7352	113.49	2.62
SCTNet*(ICCV 2023) [46]		0.1027	0.6947	109.23	11.17
SAFNet*(ECCV 2024) [27]		0.0976	0.6862	111.70	3.27
HDR-Trans(ECCV 2022) [34]	our dual-stream paradigm	0.0093	0.8923	111.24	21.60
DomainPlus(MM 2022) [62]		0.0094	0.8991	110.41	7.44
SCTNet(ICCV 2023) [46]		0.0093	0.8868	106.84	11.17
SAFNet(ECCV 2024) [27]		0.0097	0.8851	111.32	3.24
EAFNet(Ours)		0.0093	0.9071	133.16	4.32



Fig. 7: Visual comparison on Tursun’s dataset. Existing methods often produce artifacts due to luminance contrast between reference and non-reference images, while SAFNet effectively suppresses these artifacts.

complemented by improvements in SSIM- μ , indicating that our exposure-adaptive fusion strategy benefits both fidelity and structural consistency.

We further conduct cross-dataset validation, where training and testing are performed on different datasets (Table II). This setting is critical for evaluating the robustness of HDR fusion models against variations in exposure patterns, motion distributions, and scene content, thereby better reflecting real-world deployment scenarios. Our EAFNet maintains clear superiority in this challenging setting, with cross-domain gains even larger than in the intra-dataset case. For example, when trained on Kalantari and tested on Prabhakar, EAFNet achieves 39.26 dB PSNR- μ and 0.9707 SSIM- μ , surpassing the next best approach by over 1.2 dB and 0.03, respectively. This demonstrates that our model does not overfit to dataset-specific statistics, but learns exposure-aware and motion-robust fusion representations that transfer effectively across domains. The strong bidirectional results confirm the generality and domain-agnostic nature of our fusion mechanism.

Qualitative Comparisons. Fig.6 presents visual comparisons on the Prabhakar and Kalantari datasets. Most existing methods exhibit noticeable ghosting artifacts, particularly around moving objects and edges with exposure differences. In over-exposed regions, the Kalantari method suffers from detail loss, while AHDRNet and HDR-Trans produce large saturated patches, and DomainPlus struggles with color inconsistencies.

In contrast, EAFNet recovers fine structures in saturated areas while preserving natural and consistent color reproduction.

We also evaluate on challenging HDR datasets without ground truth. In Tursun’s dataset (Fig.7), large luminance differences between reference and non-reference frames often cause severe artifacts in competing methods, particularly when bright backgrounds in the reference correspond to dark content in non-reference frames. EAFNet effectively suppresses these artifacts, producing perceptually coherent HDR reconstructions.

C. HDR Video Experimental Results

Quantitative Comparisons. Table III summarizes the quantitative results. We interpret these findings from two perspectives:

Paradigm-level comparison (AE vs. our dual-stream). Dual-stream-based methods consistently achieve lower luminance standard deviation (LSD) and higher temporal SSIM (t-SSIM) than AE-based methods, indicating superior temporal stability and reduced flickering. For instance, the best AE-based method, HDRFlow, attains an LSD of 0.0914 and a t-SSIM of 0.7352, whereas our EAFNet under the dual-stream paradigm achieves 0.0093 and 0.9071, respectively. This substantial improvement stems from the fixed-exposure temporal reference in the dual-stream pipeline, which effectively eliminates inter-frame luminance flickering caused by alternating exposure in AE pipelines.

Within-dual-stream comparison (our EAFNet vs. image dehghosting baselines). When all methods operate under our dual-stream paradigm, our EAFNet outperforms all integrated image dehghosting-based baselines in both temporal and spatial quality metrics. EAFNet achieves the highest t-SSIM (0.9071) and ties for the best LSD (0.0093), reflecting its ability to simultaneously preserve temporal coherence and fine-grained spatial details. Notably, it accomplishes this while maintaining a reasonable inference time (4.32 ms for a 128×128 patch), which is faster than most transformer-based baselines.

Qualitative Comparisons. Visual comparisons in Fig. 9 and Fig. 8 further support the quantitative findings.

Paradigm-level comparison (AE vs. our dual-stream). As shown in Fig. 9, AE-based reconstructions exhibit noticeable luminance fluctuations between consecutive frames. These artifacts are inherent to AE pipelines due to the lack of a consistent exposure reference. In contrast, our results maintain



Fig. 8: Visual comparison with HDR image dehghosting methods on self-captured videos. Our EAFNet reduces ghosting from motion (first row) and background misalignment (second row), recovering natural colors and fine details in dark regions (third row).



Fig. 9: Visual comparison with AE methods on self-captured video dataset. Our dual-camera system reconstructs HDR video with consistent luminance.

stable luminance across frames and significantly reduce temporal artifacts, benefiting from the persistent medium-exposure reference stream.

Within-dual-stream comparison (our EAFNet vs. image dehghosting baselines). As shown in Fig. 8, in high-motion scenarios, some image dehghosting baselines (e.g., DomainPlus, SAFNet) generate ghosting or introduce color distortions in dark regions, whereas our EAFNet preserves spatial alignment and reproduces accurate color. Under extreme luminance contrast, EAFNet better suppresses misalignment artifacts, maintaining natural transitions in overexposed or underexposed areas. In localized low-light regions, EAFNet recovers fine structures without introducing noise, enhancing perceptual clarity. These visual improvements align with the quantitative margins in Table III, highlighting the advantage of EAFNet within the dual-stream framework.

D. Ablation study

In this section, we first evaluate the robustness of our framework under different dual-camera deployment conditions using our self-captured real-world dataset, focusing on the impact of calibration accuracy, input ordering, and frame rate. We then perform an ablation study on EAFNet to analyze the contribution of each component and the source of efficiency, with all quantitative results reported on Prabhakar's dataset [44].

TABLE IV: t-SSIM comparison under different dual-camera deployment settings. **base**: Baseline dual-camera system settings. **w/o Cal.**: Dual-camera system without calibration. **Random nr.**: Randomized input order of non-reference frames. **Lower fr.**: Lower frame rate for non-reference frame input.

Method	settings	Base.	w/o Cal.	Random nr.	Lower fr.
HDR-Trans(ECCV 2022) [34]		0.8923	0.8922	0.8926	0.8924
DomainPlus(MM 2022) [62]		0.8991	0.8994	0.8997	0.8985
SCTNet(ICCV 2023) [46]		0.8868	0.8872	0.8842	0.8871
SAFNet(ECCV 2024) [27]		0.8851	0.8861	0.8848	0.8836
EAFNet(Ours)		0.9071	0.9079	0.9072	0.9066

Dual-Camera Analysis. In a dual-camera system, imperfect calibration and potential desynchronization can lead to geometric misalignment and motion-induced misalignment, respectively. In our prototype, no special effort is made to achieve sub-pixel calibration or perfect synchronization. Instead, the fusion framework is designed to tolerate moderate deviations in both geometry and timing. The training data include dynamic scenes with motion and occlusion, allowing the model to learn robustness to such spatial inconsistencies.

Table IV reports t-SSIM under four deployment variants. Variations across deployment variants are small for all methods (≤ 0.003), indicating that, within the tested range, moderate calibration errors, input order changes, and frame-rate reductions have limited impact on temporal flickering. Minor fluctuations are likely due in part to the cropping required for alignment rather than alignment failure itself. Overall, the results suggest that, within the tested range of deviations, temporal stability can be maintained without the need for precise calibration and strict synchronization, but a higher level of calibration and synchronization may still be beneficial for optimizing performance in more demanding scenarios.

Global Luminance Alignment. We alter the composition of the input channels and configure four scenarios to investigate the impact of GLA. As shown in Table VI, the first scenario (i.e., our model) exhibits the best performance. The visualization results of the ablation experiments on GLA with Prabhakar's dataset are shown in Fig. 11, in the first row, other variants fail to restore the overexposed details of the window frame. In the second row, ghosting occurs in the

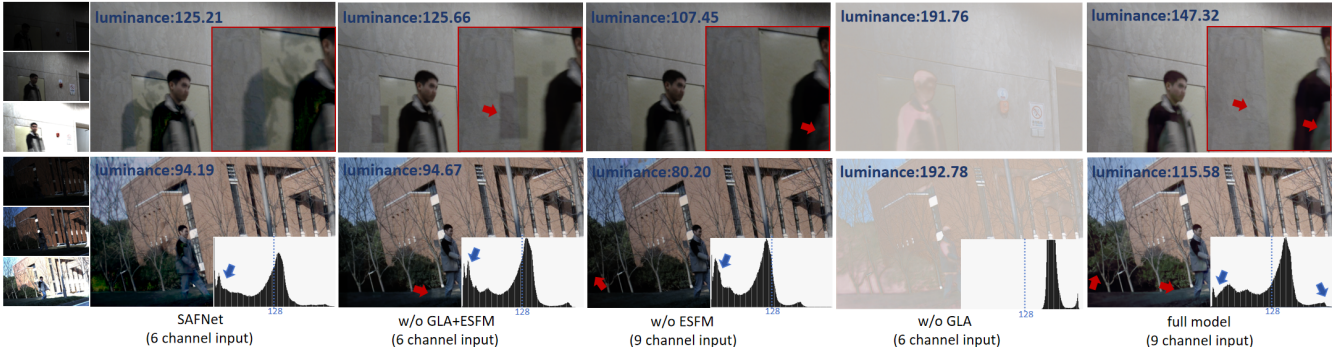


Fig. 10: Visual comparison of ablation on self-captured videos. The integration of GLA and ESFM influences the overall luminance and jointly reduces ghosting while enhancing detail in dark regions. The luminance histograms show that our method increases the visibility of extremely dark areas without causing an increase in high-luminance pixels.

TABLE V: The ablation study of pre-alignment subnetwork and asymmetric cross-feature fusion subnetwork on Prabhakar’s datasets

Method	pre align		fusion		PSNR- μ	PSNR-L	SSIM- μ	SSIM-L
	GLA	EFSM	ACA	fguide				
1	✗	✗	✓	✓	41.29	39.47	0.9728	0.9888
2	✓	✗	✓	✓	41.43	39.73	0.9722	0.9890
3	✗	✓	✓	✓	41.17	39.33	0.9726	0.9780
4	✓	✓	CA	✓	41.61	39.80	0.9726	0.9892
5	✓	✓	✓	✗	41.48	39.79	0.9723	0.9893
6	✓	✓	✗	✗	41.13	39.12	0.9708	0.9887
7	✗	✗	✗	✗	40.81	38.70	0.9703	0.9784
Ours	✓	✓	✓	✓	41.80	40.14	0.9731	0.9895



Fig. 11: The contributions of global luminance alignment. Our method effectively suppresses ghosting caused by misalignment and restores more details.

overexposed areas outside the window. The introduction of the global luminance alignment method leads to enhanced detail preservation while effectively mitigating undesirable artifacts. **Exposure-guided Feature Selection Module.** Table V presents the effectiveness of the EFSM. As shown in the first four rows, without global luminance alignment, EFSM not only fails to achieve the expected improvement but also makes a negative optimization in some cases. This can be attributed to the lack of consistent brightness information during the feature selection process, which may lead to a loss of image details.

TABLE VI: Ablation investigation about global luminance alignment.

Method	Channels	Original	Gamma Correction	GLA	PSNR- μ	PSNR-L	SSIM- μ	SSIM-L
1	6	✓	✗	✗	41.17	39.33	0.9726	0.9780
2	6	✓	✓	✓	41.08	38.97	0.9729	0.9884
3	6	✗	✓	✓	41.19	39.54	0.9729	0.9882
Ours	9	✓	✓	✓	41.80	40.14	0.9731	0.9895

TABLE VII: Experiments on changing the proportions in exposure-guided feature selection module

Method	Proportions	PSNR- μ	PSNR-L	SSIM- μ	SSIM-L
1	1:2	41.41	39.66	0.9728	0.9791
2	1:1	41.43	39.70	0.9728	0.9892
3	4:1	41.68	40.00	0.9725	0.9893
4	8:1	41.72	40.02	0.9726	0.9894
Ours	2:1	41.80	40.14	0.9731	0.9895

After introducing GLA, EFSM effectively harmonizes the brightness information, mitigating errors caused by brightness variations. As shown in Fig. 10, this integration results in a significant enhancement in detail preservation while the PSNR- μ is increased by 0.37 dB over the baseline. The luminance histograms show that the joint role of GLA and EFSM increases the visibility of extremely dark areas without causing an increase in high-luminance pixels. However, in the absence of ESFM, while some improvements are observed in intra-dataset performance (Table V), introducing GLA alone may result in overfitting and suppressing details in high-exposure images. This results in loss of details in dark areas and an overall decrease in image luminance.

We find that feature selection is notably affected by two modulation parameters: feature-guide modulation coefficients and exposure-guide modulation coefficients. To explore this effect more comprehensively, we conduct an in-depth analysis of how varying the modulation coefficient ratios influences performance. As shown in Table VII, we construct five different networks with varying modulation coefficient ratios. Among these, the 2:1 ratio achieves the highest PSNR- μ , indicating optimal performance under this configuration. As shown in Fig. 12, the proposed GLA and EFSM work collaboratively to fully explore exposure information and enhance meaningful details. Specifically, the shadow details in low-exposure features are enhanced, while the overexposed regions in high-exposure features are suppressed.

Asymmetric Cross-feature Fusion Subnetwork. As shown in Table V, replacing the asymmetric cross-feature fusion subnetwork with a generally used attention subnetwork [56] (line 7) results in a 0.67 dB drop in PSNR- μ . Fig. 14 and Fig. 13 further confirm that our method effectively mitigates misalignment artifacts. Additionally, we evaluate the role of

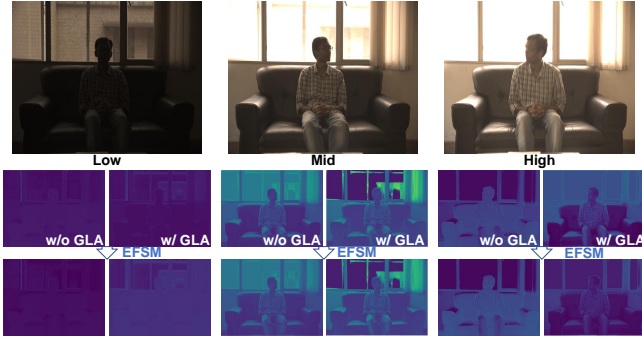


Fig. 12: Visualization of feature maps before and after ESFM. Global luminance alignment is crucial for ESFM, suppressing overexposed areas in the high-exposure input and enhancing underexposed regions in the low-exposure input.

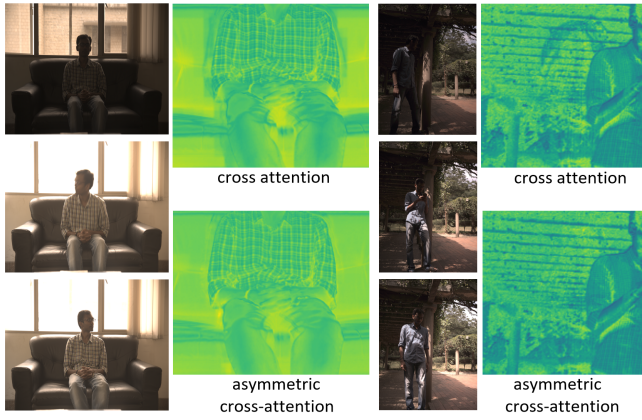


Fig. 13: Visual comparison of asymmetric cross-attention and cross-attention. Our method reduces misalignment artifacts.

the asymmetric cross-attention (ACA) by comparing it with cross-attention (CA) mechanism. The ACA improves PSNR- μ by 0.19 dB (line 5). The cross-scale guidance features f_{guide} further enhance fusion accuracy, reducing artifacts and contributing to a 0.32 dB gain in PSNR- μ .

Restoration Subnetwork. In this section, we conduct ablation experiments to evaluate the role of the frequency-domain design and multi-scale structure in HDR reconstruction. As shown in Table VIII, the baseline model (merging network in AHDNet) achieves a PSNR- μ of 40.81 and an SSIM- μ of 0.9719. First, we remove the frequency-domain design, and the results show that the PSNR- μ dropped by 0.09. Next, we perform an ablation experiment on the multi-scale structure by removing it. The results indicate that, without the multi-scale structure, the PSNR- μ decreased by 0.22. Our full model, which incorporates both the frequency-domain design and multi-scale structure, yields the highest performance, achieving a PSNR- μ of 41.80 and an SSIM- μ of 0.97311.

E. limitation

Camera parallax. The inherent fixed-baseline nature of our dual-camera system inevitably introduces parallax between the two views, especially for objects at close range. Given our hardware configuration ($B = 40\text{mm}$, $f = 6.5\text{mm}$,

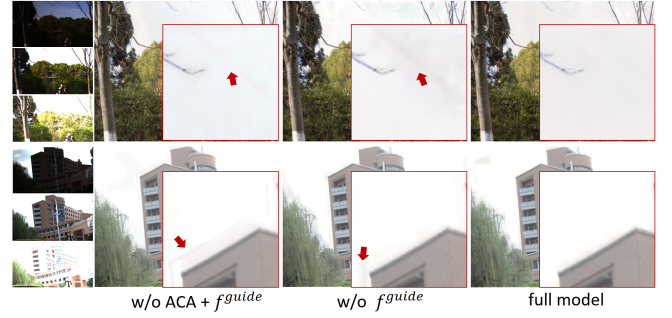


Fig. 14: Visual comparison of ablation on self-captured videos. Our method reduces most ghosting artifacts.

TABLE VIII: Comparison of the separate effects of the restoration subnetwork.

Method	model	PSNR- μ	PSNR-L	SSIM- μ	SSIM-L
1	baseline	40.81	38.60	0.9719	0.9881
2	w/o multi-scale	41.58	39.86	0.9725	0.9891
3	w/o DWT	<u>41.71</u>	<u>40.04</u>	<u>0.9729</u>	<u>0.9895</u>
Ours	full model	41.80	40.14	0.9731	0.9895

$p = 3.45\mu\text{m}$, $f_{\text{px}} \approx 1884, \text{px}$), the expected horizontal disparity for a target at distance Z follows

$$\Delta x \approx \frac{f_{\text{px}} B}{Z}. \quad (13)$$

This corresponds to ~ 9.4 pixels for targets at 8m and over 25 pixels for those at 3m. Such disparity is inherent to our system geometry and can be mitigated by reducing the camera baseline.

We analyze the impact of parallax on model performance. As shown in Fig. 15, performance degrades as parallax increases. This trend is particularly pronounced for CNN-based approaches (SAFNet and DomainPlus), which are inherently sensitive to spatial misalignments due to their limited receptive fields and lack of explicit geometry modeling. Large disparities can cause feature mismatches across views, leading to ghosting, blur, or texture loss in the fused HDR output. Nevertheless, our method consistently maintains the highest reconstruction quality across all disparity ranges, demonstrating its robustness in the presence of parallax.

Efficiency Analysis The overall efficiency of HDR video processing depends on both data acquisition throughput and reconstruction latency. Our system addresses the acquisition bottleneck by employing an asynchronous dual-camera design, which decouples the capture of varying-exposure frames from the temporally consistent reference stream. This configuration eliminates the delays typically introduced by long high-exposure frames in single-camera systems, thereby enabling real-time HDR frame acquisition.

Although the proposed reconstruction model (EAFNet) is not explicitly optimized for real-time inference, it demonstrates competitive runtime performance in practice, as summarized in Table III. The system design thus provides a practical balance between capture efficiency and reconstruction quality, supporting high-rate video acquisition with high dynamic range and temporal consistency.

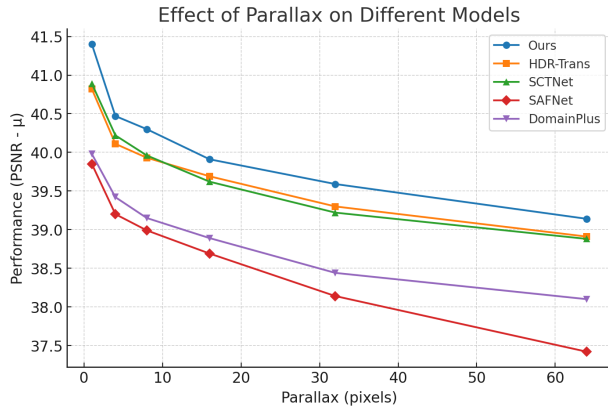


Fig. 15: Performance variation of different models under simulated parallax. The horizontal axis denotes the introduced horizontal disparity in pixels, and the vertical axis shows the performance (PSNR- μ). All methods exhibit performance degradation as disparity increases, with SAFNet and DomainPlus showing the most significant drop. Our method consistently achieves the highest reconstruction quality across the entire disparity range, demonstrating superior robustness to parallax.

VI. CONCLUSION

In this work, we revisit the fundamental cause of temporal instability in alternating-exposure (AE) HDR video, which lies in the entanglement of temporal luminance anchoring with exposure-dependent detail selection, and propose a dual-stream paradigm that explicitly decouples these two roles. Specifically, we introduce an exposure-asymmetric dual-camera system (DCS) that fixes the reference exposure to stabilize frame-to-frame luminance while allowing the auxiliary stream to vary exposure for capturing high dynamic range details. To support this system, we design EAFNet to effectively suppress ghosting artifacts while preserving fine details in real-world scenes. Extensive experiments on multiple datasets and real-world sequences demonstrate that the proposed paradigm improves both temporal stability and reconstruction quality compared with AE-based baselines and HDR image deghosting methods, while remaining cost-efficient and deployment-friendly. Our dual-stream solution provides a promising direction for real-time HDR video capture.

REFERENCES

- [1] Luca Bogoni. Extending dynamic range of monochrome and color images through fusion. In *Proceedings 15th International Conference on Pattern Recognition. ICPR-2000*, volume 3, pages 7–12. IEEE, 2000.
- [2] Guanying Chen, Chaofeng Chen, Shi Guo, Zhetong Liang, Kwan-Yee K Wong, and Lei Zhang. Hdr video reconstruction: A coarse-to-fine network and a real-world benchmark dataset. In *Proceedings of the IEEE/CVF international conference on computer vision*, pages 2502–2511, 2021.
- [3] Jie Chen, Zaifeng Yang, Tsz Nam Chan, Hui Li, Junhui Hou, and Lap-Pui Chau. Attention-guided progressive

- neural texture fusion for high dynamic range image restoration. *IEEE Transactions on Image Processing*, 31:2661–2672, 2022.
- [4] Rufeng Chen, Bolun Zheng, Hua Zhang, Quan Chen, Chenggang Yan, Gregory Slabaugh, and Shanxin Yuan. Improving dynamic hdr imaging with fusion transformer. In *Proceedings of the AAAI Conference on Artificial Intelligence*, volume 37, pages 340–349, 2023.
- [5] Ming Cheng, Zhan Ma, M Salman Asif, Yiling Xu, Haojie Liu, Wenbo Bao, and Jun Sun. A dual camera system for high spatiotemporal resolution video acquisition. *IEEE Transactions on Pattern Analysis and Machine Intelligence*, 43(10):3275–3291, 2020.
- [6] Ming Cheng, Yiling Xu, Wang Shen, M Salman Asif, Chao Ma, Jun Sun, and Zhan Ma. H 2-stereo: High-speed, high-resolution stereoscopic video system. *IEEE Transactions on Broadcasting*, 68(4):886–903, 2022.
- [7] Inchang Choi, Seung-Hwan Baek, and Min H Kim. Reconstructing interlaced high-dynamic-range video using joint learning. *IEEE Transactions on Image Processing*, 26(11):5353–5366, 2017.
- [8] Haesoo Chung and Nam Ik Cho. Lan-hdr: Luminance-based alignment network for high dynamic range video reconstruction. In *Proceedings of the IEEE/CVF International Conference on Computer Vision*, pages 12760–12769, 2023.
- [9] Jiahao Cui, Wei Jiang, Zhan Peng, Zhiyu Pan, and Zhiguo Cao. Exposure completing for temporally consistent neural high dynamic range video rendering. In *Proceedings of the 32nd ACM International Conference on Multimedia*, pages 10027–10035, 2024.
- [10] Paul E Debevec and Jitendra Malik. Recovering high dynamic range radiance maps from photographs. In *ACM SIGGRAPH 2008 classes*, pages 1–10. 2008.
- [11] Xuan Dong, Xiaoyan Hu, Weixin Li, Xiaojie Wang, and Yunhong Wang. Miehdr cnn: Main image enhancement based ghost-free high dynamic range imaging using dual-lens systems. In *Proceedings of the AAAI Conference on Artificial Intelligence*, volume 35, pages 1264–1272, 2021.
- [12] Thorsten Grosch et al. Fast and robust high dynamic range image generation with camera and object movement. *Vision, Modeling and Visualization, RWTH Aachen*, 277284(3):2, 2006.
- [13] Yulia Gryaditskaya, Tania Pouli, Erik Reinhard, Karol Myszkowski, and Hans-Peter Seidel. Motion aware exposure bracketing for hdr video. In *Computer Graphics Forum*, volume 34, pages 119–130. Wiley Online Library, 2015.
- [14] Jin Han, Chu Zhou, Peiqi Duan, Yehui Tang, Chang Xu, Chao Xu, Tiejun Huang, and Boxin Shi. Neuromorphic camera guided high dynamic range imaging. In *Proceedings of the IEEE/CVF Conference on Computer Vision and Pattern Recognition*, pages 1730–1739, 2020.
- [15] Felix Heide, Markus Steinberger, Yun-Ta Tsai, Mushfiquar Rouf, Dawid Pajkak, Dikpal Reddy, Orazio Gallo, Jing Liu, Wolfgang Heidrich, Karen Egiazarian, et al. Flexisp: A flexible camera image processing framework. *ACM*

- Transactions on Graphics (ToG)*, 33(6):1–13, 2014.
- [16] Yong Seok Heo, Kyoung Mu Lee, Sang Uk Lee, Youngsu Moon, and Joonhyuk Cha. Ghost-free high dynamic range imaging. In *Asian Conference on Computer Vision*, pages 486–500. Springer, 2010.
 - [17] Jun Hu, Orazio Gallo, Kari Pulli, and Xiaobai Sun. Hdr deghosting: How to deal with saturation? In *Proceedings of the IEEE Conference on Computer Vision and Pattern Recognition*, pages 1163–1170, 2013.
 - [18] Katrien Jacobs, Celine Loscos, and Greg Ward. Automatic high-dynamic range image generation for dynamic scenes. *IEEE Computer Graphics and Applications*, 28(2):84–93, 2008.
 - [19] Katrien Jacobs, Celine Loscos, and Greg Ward. Automatic high-dynamic range image generation for dynamic scenes. *IEEE Computer Graphics and Applications*, 28(2):84–93, 2008.
 - [20] Yitong Jiang, Inchang Choi, Jun Jiang, and Jinwei Gu. Hdr video reconstruction with tri-exposure quad-bayer sensors. *arXiv preprint arXiv:2103.10982*, 2021.
 - [21] Nima Khademi Kalantari and Ravi Ramamoorthi. Deep hdr video from sequences with alternating exposures. In *Computer graphics forum*, volume 38, pages 193–205. Wiley Online Library, 2019.
 - [22] Nima Khademi Kalantari, Ravi Ramamoorthi, et al. Deep high dynamic range imaging of dynamic scenes. *ACM Trans. Graph.*, 36(4):144–1, 2017.
 - [23] Nima Khademi Kalantari, Ravi Ramamoorthi, et al. Deep high dynamic range imaging of dynamic scenes. *ACM Trans. Graph.*, 36(4):144–1, 2017.
 - [24] Nima Khademi Kalantari, Eli Shechtman, Connelly Barnes, Soheil Darabi, Dan B Goldman, and Pradeep Sen. Patch-based high dynamic range video.
 - [25] Sing Bing Kang, Matthew Uyttendaele, Simon Winder, and Richard Szeliski. High dynamic range video. *ACM Transactions on Graphics (TOG)*, 22(3):319–325, 2003.
 - [26] Diederik P Kingma and Jimmy Ba. Adam: A method for stochastic optimization. *arXiv preprint arXiv:1412.6980*, 2014.
 - [27] Lingtong Kong, Bo Li, Yike Xiong, Hao Zhang, Hong Gu, and Jinwei Chen. Safnet: Selective alignment fusion network for efficient hdr imaging. In *European Conference on Computer Vision*, pages 256–273. Springer, 2024.
 - [28] Joel Kronander, Stefan Gustavson, Gerhard Bonnet, Anders Ynnerman, and Jonas Unger. A unified framework for multi-sensor hdr video reconstruction. *Signal Processing: Image Communication*, 29(2):203–215, 2014.
 - [29] Bruno Lecouat, Thomas Eboli, Jean Ponce, and Julien Mairal. High dynamic range and super-resolution from raw image bursts. *arXiv preprint arXiv:2207.14671*, 2022.
 - [30] Ru Li, Chuan Wang, Jue Wang, Guanghui Liu, Heng-Yu Zhang, Bing Zeng, and Shuaicheng Liu. Uphdr-gan: Generative adversarial network for high dynamic range imaging with unpaired data. *IEEE Transactions on Circuits and Systems for Video Technology*, 32(11):7532–7546, 2022.
 - [31] Weixin Li, Tiantian Cao, Chang Liu, Xue Tian, Ya Li, Xiaojie Wang, and Xuan Dong. Dual-lens hdr using guided 3d exposure cnn and guided denoising transformer. *ACM Transactions on Multimedia Computing, Communications and Applications*, 19(5):1–20, 2023.
 - [32] Yuelong Li, Chul Lee, and Vishal Monga. A maximum a posteriori estimation framework for robust high dynamic range video synthesis. *IEEE Transactions on Image Processing*, 26(3):1143–1157, 2016.
 - [33] Zhen Liu, Wenjie Lin, Xinpeng Li, Qing Rao, Ting Jiang, Mingyan Han, Haoqiang Fan, Jian Sun, and Shuaicheng Liu. Adnet: Attention-guided deformable convolutional network for high dynamic range imaging. In *Proceedings of the IEEE/CVF Conference on Computer Vision and Pattern Recognition*, pages 463–470, 2021.
 - [34] Zhen Liu, Yinglong Wang, Bing Zeng, and Shuaicheng Liu. Ghost-free high dynamic range imaging with context-aware transformer. In *European Conference on Computer Vision*, pages 344–360. Springer, 2022.
 - [35] Stephen Mangiat and Jerry Gibson. High dynamic range video with ghost removal. In *Applications of digital image processing XXXIII*, volume 7798, pages 307–314. SPIE, 2010.
 - [36] Stephen Mangiat and Jerry Gibson. Spatially adaptive filtering for registration artifact removal in hdr video. In *2011 18th IEEE International Conference on Image Processing*, pages 1317–1320. IEEE, 2011.
 - [37] Rafał Mantiuk, Kil Joong Kim, Allan G Rempel, and Wolfgang Heidrich. Hdr-vdp-2: A calibrated visual metric for visibility and quality predictions in all luminance conditions. *ACM Transactions on graphics (TOG)*, 30(4):1–14, 2011.
 - [38] Julien NP Martel, Lorenz K Mueller, Stephen J Carey, Piotr Dudek, and Gordon Wetzstein. Neural sensors: Learning pixel exposures for hdr imaging and video compressive sensing with programmable sensors. *IEEE Transactions on Pattern Analysis and Machine Intelligence*, 42(7):1642–1653, 2020.
 - [39] Morgan McGuire, Wojciech Matusik, Hanspeter Pfister, Billy Chen, John F Hughes, and Shree K Nayar. Optical splitting trees for high-precision monocular imaging. *IEEE Computer Graphics and Applications*, 27(2):32–42, 2007.
 - [40] Shree K Nayar and Tomoo Mitsunaga. High dynamic range imaging: Spatially varying pixel exposures. In *Proceedings IEEE Conference on Computer Vision and Pattern Recognition. CVPR 2000 (Cat. No. PR00662)*, volume 1, pages 472–479. IEEE, 2000.
 - [41] Yuzhen Niu, Jianbin Wu, Wenxi Liu, Wenzhong Guo, and Rynson WH Lau. Hdr-gan: Hdr image reconstruction from multi-exposed ldr images with large motions. *IEEE Transactions on Image Processing*, 30:3885–3896, 2021.
 - [42] Feiyue Peng, Maojun Zhang, Shiming Lai, Hanlin Tan, and Shen Yan. Deep hdr reconstruction of dynamic scenes. In *2018 IEEE 3rd International Conference on Image, Vision and Computing (ICIVC)*, pages 347–351. IEEE, 2018.
 - [43] K Ram Prabhakar, Susmit Agrawal, Durgesh Kumar

- Singh, Balraj Ashwath, and R Venkatesh Babu. Towards practical and efficient high-resolution hdr deghosting with cnn. In *Computer Vision–ECCV 2020: 16th European Conference, Glasgow, UK, August 23–28, 2020, Proceedings, Part XXI 16*, pages 497–513. Springer, 2020.
- [44] K Ram Prabhakar, Rajat Arora, Adhitya Swaminathan, Kunal Pratap Singh, and R Venkatesh Babu. A fast, scalable, and reliable deghosting method for extreme exposure fusion. In *2019 IEEE International Conference on Computational Photography (ICCP)*, pages 1–8. IEEE, 2019.
- [45] Pradeep Sen, Nima Khademi Kalantari, Maziar Yaesoubi, Soheil Darabi, Dan B Goldman, and Eli Shechtman. Robust patch-based hdr reconstruction of dynamic scenes. *ACM Trans. Graph.*, 31(6):203–1, 2012.
- [46] Steven Tel, Zongwei Wu, Yulun Zhang, Barthelemy Heyrman, Cedric Demonceaux, Radu Timofte, and Dominique Ginjac. Alignment-free hdr deghosting with semantics consistent transformer. In *2023 IEEE/CVF International Conference on Computer Vision (ICCV)*, pages 12790–12799. IEEE Computer Society, 2023.
- [47] Michael D Tocci, Chris Kiser, Nora Tocci, and Pradeep Sen. A versatile hdr video production system. *ACM Transactions on Graphics (TOG)*, 30(4):1–10, 2011.
- [48] Okan Tarhan Tursun, Ahmet Oğuz Akyüz, Aykut Erdem, and Erkut Erdem. An objective deghosting quality metric for hdr images. In *Computer Graphics Forum*, volume 35, pages 139–152. Wiley Online Library, 2016.
- [49] Caixin Wang, Jie Zhang, Matthew A. Wilson, and Ralph Etienne-Cummings. Pix2hdr - a pixel-wise acquisition and deep learning-based synthesis approach for high-speed hdr videos. *IEEE Transactions on Pattern Analysis and Machine Intelligence*, 46(12):8771–8787, 2024.
- [50] Caixin Wang, Jie Zhang, Matthew A Wilson, and Ralph Etienne-Cummings. Pix2hdr-a pixel-wise acquisition and deep learning-based synthesis approach for high-speed hdr videos. *IEEE Transactions on Pattern Analysis and Machine Intelligence*, 46(12):8771–8787, 2024.
- [51] Lin Wang and Kuk-Jin Yoon. Deep learning for hdr imaging: State-of-the-art and future trends. *IEEE Transactions on Pattern Analysis and Machine Intelligence*, 44(12):8874–8895, 2021.
- [52] Zhou Wang, Alan C Bovik, Hamid R Sheikh, and Eero P Simoncelli. Image quality assessment: from error visibility to structural similarity. *IEEE transactions on image processing*, 13(4):600–612, 2004.
- [53] Shangzhe Wu, Jiarui Xu, Yu-Wing Tai, and Chi-Keung Tang. End-to-end deep hdr imaging with large foreground motions. In *European Conference on Computer Vision*, volume 1, 2018.
- [54] Gangwei Xu, Yujin Wang, Jinwei Gu, Tianfan Xue, and Xin Yang. Hdrflow: Real-time hdr video reconstruction with large motions. In *Proceedings of the IEEE/CVF Conference on Computer Vision and Pattern Recognition*, pages 24851–24860, 2024.
- [55] Qingsen Yan, Weiye Chen, Song Zhang, Yu Zhu, Jinqiu Sun, and Yanning Zhang. A unified hdr imaging method with pixel and patch level. In *Proceedings of the IEEE/CVF Conference on Computer Vision and Pattern Recognition*, pages 22211–22220, 2023.
- [56] Qingsen Yan, Dong Gong, Qinfeng Shi, Anton van den Hengel, Chunhua Shen, Ian Reid, and Yanning Zhang. Attention-guided network for ghost-free high dynamic range imaging. In *Proceedings of the IEEE/CVF Conference on Computer Vision and Pattern Recognition*, pages 1751–1760, 2019.
- [57] Qingsen Yan, Bo Wang, Lei Zhang, Jingyu Zhang, Zheng You, Qinfeng Shi, and Yanning Zhang. Towards accurate hdr imaging with learning generator constraints. *Neuro-computing*, 428:79–91, 2021.
- [58] Qingsen Yan, Kangzhen Yang, Tao Hu, Genggeng Chen, Kexin Dai, Peng Wu, Wenqi Ren, and Yanning Zhang. From dynamic to static: Stepwisely generate hdr image for ghost removal. *IEEE Transactions on Circuits and Systems for Video Technology*, 2024.
- [59] Wei Zhang and Wai-Kuen Cham. Gradient-directed multiexposure composition. *IEEE Transactions on Image Processing*, 21(4):2318–2323, 2011.
- [60] Zhengyou Zhang. A flexible new technique for camera calibration. *IEEE Transactions on Pattern Analysis and Machine Intelligence*, 22(11):1330–1334, 2002.
- [61] Hang Zhao, Boxin Shi, Christy Fernandez-Cull, Sai-Kit Yeung, and Ramesh Raskar. Unbounded high dynamic range photography using a modulo camera. In *2015 IEEE International Conference on Computational Photography (ICCP)*, pages 1–10. IEEE, 2015.
- [62] Bolun Zheng, Xiaokai Pan, Hua Zhang, Xiaofei Zhou, Gregory Slabaugh, Chenggang Yan, and Shanxin Yuan. Domainplus: Cross transform domain learning towards high dynamic range imaging. In *Proceedings of the 30th ACM International Conference on Multimedia*, pages 1954–1963, 2022.
- [63] Bolun Zheng, Shanxin Yuan, Chenggang Yan, Xiang Tian, Jiyong Zhang, Yaoqi Sun, Lin Liu, Aleš Leonardis, and Gregory Slabaugh. Learning frequency domain priors for image demoiréing. *IEEE Transactions on Pattern Analysis and Machine Intelligence*, 44(11):7705–7717, 2021.